DEFENSE TECHNICAL INFORMATION CENTER

Information for the Defense Community

DTIC® has determined on 06/19/2009 that this Technical Document has the Distribution Statement checked below. The current distribution for this document can be found in the DTIC® Technical Report Database.

☒ **DISTRIBUTION STATEMENT A.** Approved for public release; distribution is unlimited.

☐ **© COPYRIGHTED**; U.S. Government or Federal Rights License. All other rights and uses except those permitted by copyright law are reserved by the copyright owner.

☐ **DISTRIBUTION STATEMENT B.** Distribution authorized to U.S. Government agencies only (fill in reason) (date of determination). Other requests for this document shall be referred to (insert controlling DoD office)

☐ **DISTRIBUTION STATEMENT C.** Distribution authorized to U.S. Government Agencies and their contractors (fill in reason) (date of determination). Other requests for this document shall be referred to (insert controlling DoD office)

☐ **DISTRIBUTION STATEMENT D.** Distribution authorized to the Department of Defense and U.S. DoD contractors only (fill in reason) (date of determination). Other requests shall be referred to (insert controlling DoD office).

☐ **DISTRIBUTION STATEMENT E.** Distribution authorized to DoD Components only (fill in reason) (date of determination). Other requests shall be referred to (insert controlling DoD office).

☐ **DISTRIBUTION STATEMENT F.** Further dissemination only as directed by (inserting controlling DoD office) (date of determination) or higher DoD authority.

Distribution Statement F is also used when a document does not contain a distribution statement and no distribution statement can be determined.

☐ **DISTRIBUTION STATEMENT X.** Distribution authorized to U.S. Government Agencies and private individuals or enterprises eligible to obtain export-controlled technical data in accordance with DoDD 5230.25; (date of determination). DoD Controlling Office is (insert controlling DoD office).

Appendix [N]

Available online at www.sciencedirect.com
ScienceDirect
ELSEVIER
International Journal of Impact Engineering 35 (2008) 920–936
INTERNATIONAL JOURNAL OF IMPACT ENGINEERING
www.elsevier.com/locate/ijimpeng

Impact response of sandwich plates with a pyramidal lattice core

Christian J. Yungwirth[a], Haydn N.G. Wadley[a], John H. O'Connor[b], Alan J. Zakraysek[b], Vikram S. Deshpande[c,*]

[a]*Department of Material Science & Engineering, School of Engineering and Applied Science, University of Virginia, Charlottesville, VA 22903, USA*
[b]*Naval Surface Warfare Center, Indian Head, MD 20640, USA*
[c]*Department of Engineering, Cambridge University, Trumpington Street, Cambridge CB2 1PZ, UK*

Received 29 April 2007; accepted 16 July 2007
Available online 20 July 2007

Abstract

The ballistic performance edge clamped 304 stainless-steel sandwich panels has been measured by impacting the plates at mid-span with a spherical steel projectile whose impact velocity ranged from 250 to 1300 m s^{-1}. The sandwich plates comprised two identical face sheets and a pyramidal truss core: the diameter of the impacting spherical projectile was approximately half the 25 mm truss core cell size. The ballistic behavior has been compared with monolithic 304 stainless-steel plates of approximately equal areal mass and with high-strength aluminum alloy (6061-T6) sandwich panels of identical geometry. The ballistic performance is quantified in terms of the entry and exit projectile velocities while high-speed photography is used to investigate the dynamic deformation and failure mechanisms. The stainless-steel sandwich panels were found to have a much higher ballistic resistance than the 6061-T6 aluminum alloy panels on a per volume basis but the ballistic energy absorption of the aluminum structures was slightly higher on a per unit mass basis. The ballistic performance of the monolithic and sandwich panels is almost identical though the failure mechanics of these two types of structures are rather different. At high impact velocities, the monolithic plates fail by ductile hole enlargement. By contrast, only the proximal face sheet of the sandwich plate undergoes this type of failure. The distal face sheet fails by a petalling mode over the entire velocity range investigated here. Given the substantially higher blast resistance of sandwich plates compared to monolithic plates of equal mass, we conclude that sandwich plates display a potential to outperform monolithic plates in multi-functional applications that combine blast resistance and ballistic performance.

Keywords: Impact; Pyramidal truss; Air shock waves; Energy absorption; Ballistic performance

1. Introduction

It is well known that sandwich plates possess a superior bending stiffness and strength to monolithic beams of the same mass under quasi-static loading. Theoretical studies by Fleck and Deshpande [1] and Xue and Hutchinson [2] also predicted that sandwich beams have superior shock resistance to monolithic beams. Subsequently, several experimental studies [3–5] have confirmed these initial theoretical and numerical predictions. Typically, blast events in air are accompanied by high-velocity fragments, but little is known about the ballistic resistance of these sandwich beams. Here we present an experimental investigation that compares the ballistic performance of sandwich and monolithic plates of equal areal mass.

Over the last decade, a number of new core topologies for sandwich panels have emerged. These include metallic foams [6], truss-like lattice materials (Fig. 1), prismatic sandwich cores such as the corrugated and Y-frame cores [7] and various honeycomb cores. The truss-like cores due to their open-cell architecture are ideally suited for multi-functional applications that include combined thermal and structural functionality. In this study, we focus on sandwich plates with the pyramidal truss core.

Sandwich panel structures investigated can be thought of as a pair of thin metal plates separated by a lattice of slender trusses. The penetration of thin ductile plates (those where the plate thickness is small compared with the projectile diameter) by spherical tipped projectiles can

*Corresponding author. Tel.: +44 1223 332664; fax: +44 1223 332662.
E-mail address: vsd@eng.cam.ac.uk (V.S. Deshpande).

0734-743X/$ - see front matter © 2007 Elsevier Ltd. All rights reserve
doi:10.1016/j.ijimpeng.2007.07.001

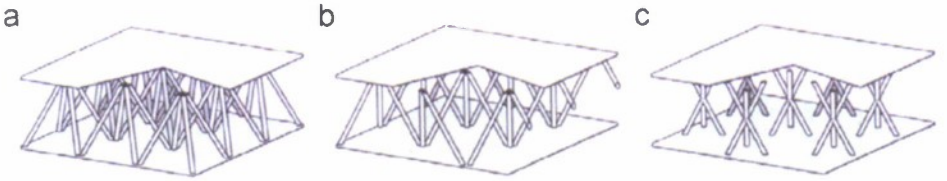

Fig. 1. Examples of truss-like lattice structures configured as the cores of sandwich panel structures: (a) pyramidal, (b) tetrahedral and (c) double layer Kagomé lattice trusses.

occur by either petalling or adiabatic shearing (plugging), sometimes in combination with ductile hole enlargement at high impact velocities [8]. Petalling usually occurs in soft materials with high work hardening rates penetrated by low-velocity projectiles. It begins with a dishing deformation of the plate which develops high circumferential strains beneath the impact location. These high strains lead to radial tensile stretching and fractures of the metal plate leading to the formation of typically 4–7 petals that bend away from the incoming projectile. Energy is dissipated by the global dishing and tearing of the plate along with the bending of the petals [9,10]. High-velocity penetration of high dynamic strength and low work hardening rate metal plates occurs by shear banding. The shear failure is confined to a thin cylindrical sheath beneath the edge of the projectile [11]. If the rise in temperature within the band causes more local softening than the increase in flow stress due to strain and strain-rate hardening, adiabatic shear bands form [12]. The metal plug is usually thinner than the original plate thickness because of radial metal flow from beneath the projectile.

The penetration of a metal sheet by a normal incidence projectile has been widely studied; see [8,13] for a recent review of the literature. Experimental studies by Almohandes et al. [14] indicated that distributing the mass of a plate between a pair of identical plates resulted in a lowering of the ballistic resistance of the system compared to a monolithic structure of equal areal mass. However, theoretical studies by Ben-Dor et al. [15] and experimental studies by Radin and Goldsmith [16] indicate little effect. Relatively few experimental studies have investigated the ballistic resistance of metallic sandwich plates. A study by Goldsmith et al. [17] concentrated on aluminum panels with honeycomb cores while Zhao et al. [18] have investigated the perforation of aluminum foam core panels. The ballistic performance of sandwich plates compared to monolithic plates of equal areal mass is as yet not clearly understood and the role of the parent material of the sandwich plates has not been clearly elucidated.

The outline of this paper is as follows. First we briefly review the use of penetration mechanism maps to explain the role of projectile mass and velocity on the failure mechanisms of ductile plates and to illustrate the effect of material layering on the ballistic performance. Second, the fabrication of stainless-steel and aluminum sandwich plates with a pyramidal truss core is described along with the ballistic testing procedure. We then summarize the measured ballistic performance of the sandwich and monolithic plates and use high-speed photographs to elucidate the deformation and failure mechanisms. We finally conclude the study by showing that stainless sandwich panels have a similar ballistic performance to monolithic plates of equal areal density even though the mechanisms of penetration are different.

2. Penetration mechanism maps

Deshpande et al. [19] have recently developed penetration mechanism maps in order to elucidate the coupling between projectile mass and velocity in determining the ballistic performance of clamped beams impacted by rigid projectiles. Here we briefly review their findings in order to (i) put the experimental observations of this study in context and (ii) help explain some of the observations discussed in Section 4.

Consider a clamped beam of span $2L$ and thickness h made from a rigid ideally plastic solid of dynamic yield strength σ_Y and density ρ. This beam is impacted at mid-span by a rigid projectile of mass G per unit thickness perpendicular to the plane of the beam. Deshpande et al. [19] considered the two critical failure modes: (a) tensile tearing and (b) shear-off. Regimes of dominance of the two failure regimes for an assumed beam material tensile failure strain $\varepsilon_f = 10\%$ and a critical normalized shear displacement $w_s^{crit}/h = 1.0$ are illustrated in the map in Fig. 2a using axes of the non-dimensional projectile impact velocity $\bar{v}_p \equiv v_p/\sqrt{\sigma_Y/\rho}$ and non-dimensional projectile mass $\bar{G} \equiv G/(\rho h^2)$. The shear-off regime is essentially insensitive to the beam aspect ratio L/h. However, tensile failure is strongly dependent on the value of L/h: with increasing L/h the regime over which tensile failure is the dominant failure mechanism shrinks and the tensile failure regime marked in Fig. 2a is only valid for the choice $L/h = 5$. The key features of the failure mechanism map are

(i) The critical penetration velocities (or the ballistic limit) decrease with increasing $\bar{G}$ as both the shear-off and tensile failure modes become more likely.
(ii) For the choices of material failure parameters made here, tensile failure is not an operative failure mechanism for $\bar{G} < 8$ and if penetration occurs, shear-off is expected to be the failure mode.

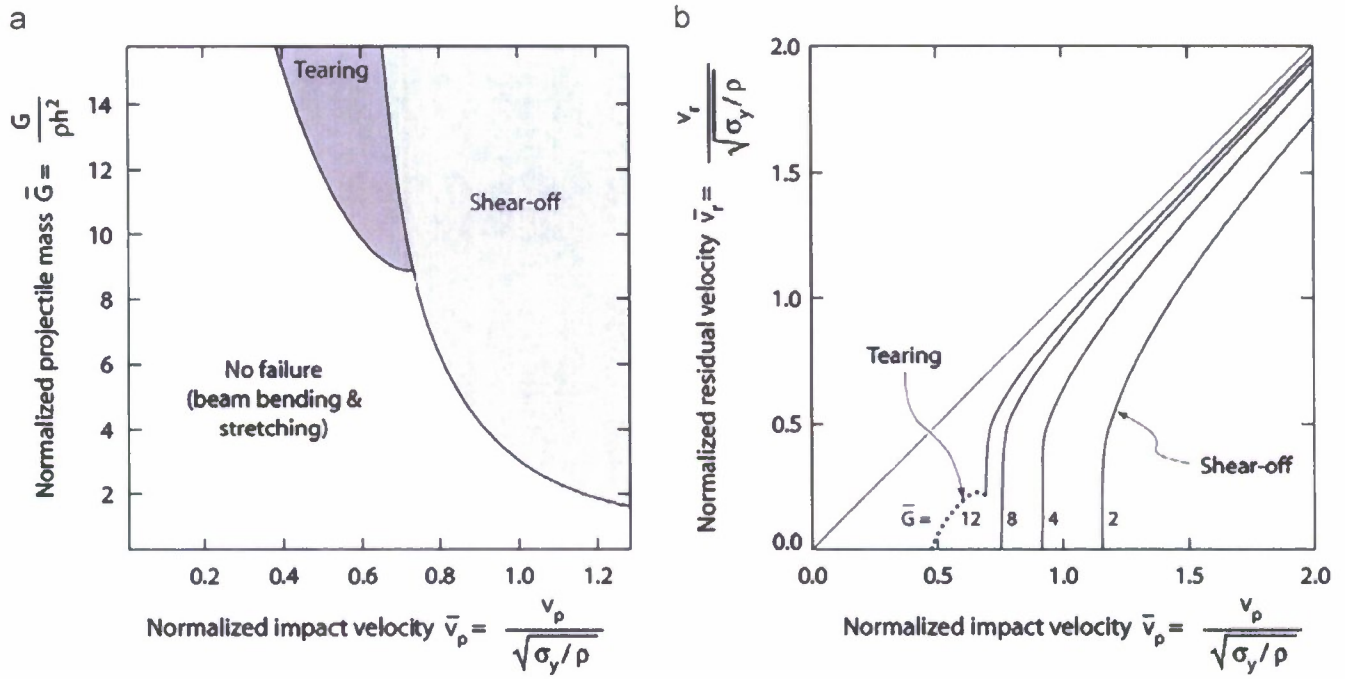

Fig. 2. (a) Failure mechanism map for the central impact of a rigid projectile against a clamped beam with an aspect ratio $L/h = 5$. The map is plotted using axes of the normalized projectile mass $\bar{G}$ and normalized projectile velocity $\bar{v}_p$. The beam material is assumed to have a tensile failure strain $\varepsilon_f = 10\%$ and critical normalized shear displacement $w_s^{crit}/h = 1.0$. (b) Predictions of the corresponding normalized projectile residual or exit velocity $\bar{v}_r$ as a function of $\bar{v}_p$ for selected value of $\bar{G}$.

(iii) For a given value of $\bar{G} \geqslant 8$, the failure mechanism transitions from shear-off to tensile failure with decreasing projectile velocity $\bar{v}_p$.

The corresponding predictions of the projectile residual or exit velocity $\bar{v}_r \equiv v_r/\sqrt{\sigma_Y/\rho}$ as a function of the impact velocity $\bar{v}_p$ are shown in Fig. 2b for four selected values of the normalized projectile mass $\bar{G}$ and the material failure parameters employed for constructing the map in Fig. 2a. The predicted failure mechanisms are indicated on these residual velocity curves and consistent with the map in Fig. 2a, tensile failure is only operational for high values of $\bar{G}$ at low impact velocities. Note that when shear-off is the failure mode, a sharp increase in the residual velocity is predicted at the critical penetration velocity. This is rationalized as follows. Just below the critical penetration velocity, the shearing in the beam under the projectile arrests just prior to the shear failure of the beam. The projectile at this instant has some residual velocity and this kinetic energy of the projectile is absorbed by the stretching and bending of the beam. At a projectile velocity just above the critical penetration velocity, shear failure of the beam prevents this additional energy absorption mechanism and the projectile penetrates with a significant proportion of the initial kinetic energy still not being dissipated. This gives the sharp increase in $\bar{v}_r$ just above the ballistic limit.

These maps illustrate the effect of the beam material density (and/or thickness and material density) on the ballistic performance of plates. Consider a beam of fixed aspect ratio L/h and areal mass $m = \rho h$. In order to understand the effect of ρ, all other parameters are held fixed including the yield strength σ_Y, material failure parameters (ε_f and w_s^{crit}/h), projectile mass G,and impact velocity v_p. The y-axis of the map in Fig. 2a can then be interpreted as $\bar{G} \equiv G\rho/m^2$. Thus, reducing the material density implies that both the normalized mass $\bar{G} \equiv G\rho/m^2$ and the normalized impact velocity $\bar{v}_p$ are reduced: this would in effect increase the ballistic performance of the beam. A practical realization of such a scenario would be the substitution of high-strength aluminum for a carbon steel beam material. Both these materials have approximately the same yield strength and failure properties but the density of aluminum is about one-third the density of steel.

2.1. Effect of material layering

The main focus of this article is to investigate the ballistic resistance of sandwich panels. To motivate this we contrast the ballistic performance of the two systems illustrated in Fig. 3 and made from a material of density ρ and yield strength σ_Y: (i) a monolithic clamped beam of thickness h and span $2L$ and (ii) a sandwich-like configuration comprising two identical but independent monolithic clamped beams each with a span $2L$ but thickness $h/2$. Thus, both the systems have equal mass and span and differ only in the way mass is spatially distributed. A

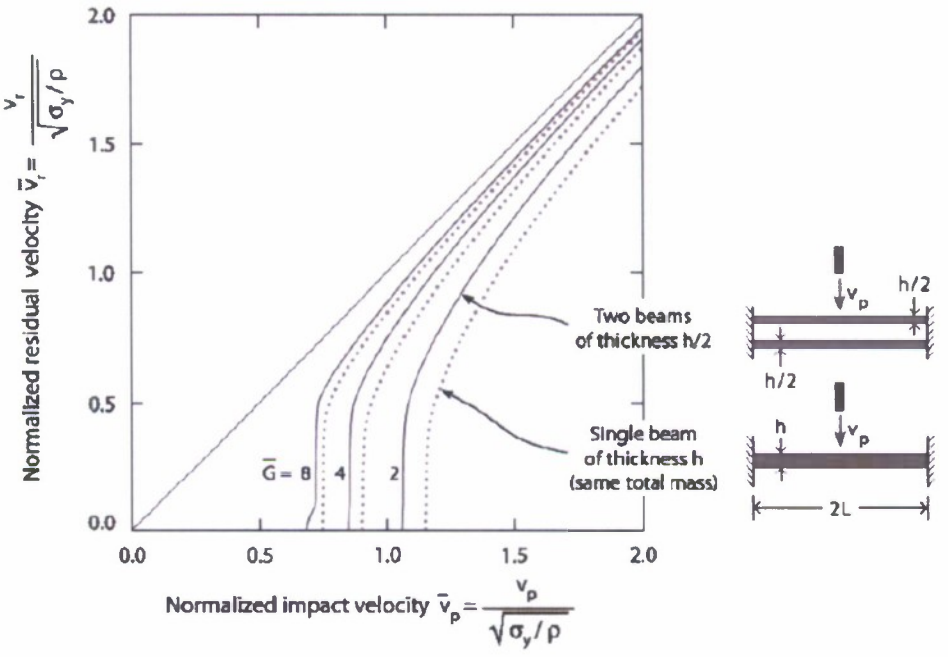

Fig. 3. Sketches of the monolithic and bilayer systems of equal mass and predictions comparing the ballistic performance (in terms of the projectile residual versus entry velocity) of the monolithic and bilayer systems. The assumed material failure parameters are $\varepsilon_f = 10\%$ and $w_s^{crit}/h = 1.0$ with predictions shown for selected values of $\bar{G}$.

projectile of mass G impacts these two configurations at mid-span as shown in Fig. 3.

Predictions of the normalized residual velocity $\bar{v}_r$ versus impact velocity $\bar{v}_p$ for the two systems are included in Fig. 3 for three selected values of the normalized projectile mass $\bar{G} \equiv G/(\rho h^2)$. The material failure parameters are the same as those used above, i.e., $\varepsilon_f = 10\%$ and the critical shearing displacements $w_s^{crit}/h = 1.0$ and $w_s^{crit}/(h/2) = 1.0$ for the monolithic and sandwich-like configurations, respectively. The predictions indicate that the ballistic performance of both the configurations is very similar with the monolithic beam performing slightly better than the sandwich-like configuration.

3. Experimental investigation

Clamped sandwich plates with a pyramidal truss core were impacted normally (zero obliquity) and centrally with spherical steel balls. The aims of the experimental investigation are as follows.

(i) To compare the ballistic performance of sandwich and monolithic plates of equal mass.
(ii) To investigate the effect of material choice on the ballistic performance of structures. Here we compare the ballistic performance of sandwich plates made from 304 stainless steel and a high-strength aluminum alloy.
(iii) To elucidate the mechanisms of failure and penetration in the sandwich plates and monolithic plates.

3.1. Construction of lattice core sandwich plates

Sandwich plates with a pyramidal truss core were manufactured from 304 stainless steel and an age-hardened 6061-T6 aluminum alloy with densities $\rho = 8000$ and $2700\,kg\,m^{-3}$, respectively. The sandwich plates comprised two identical face sheets of thickness $h = 1.5\,mm$ and a pyramidal core of thickness $c = 25.4\,mm$; see Fig. 4 for detailed dimensions of the sandwich plates. The pyramidal cores had a relative density (ratio of the effective density of the "smeared-out" core to the density of the solid material from which it is made) $\bar{\rho} = 2.6\%$ which implies that the net areal mass $m = (2h + c\bar{\rho})\rho$ of the 304 stainless-steel and aluminum alloy sandwich plates was 29.3 and $9.88\,kg\,m^{-2}$, respectively.

The pyramidal lattice cores comprised struts of length 31.75 mm and cross-section $1.9 \times 1.9\,mm^2$ as shown in Fig. 4. The cores were manufactured from 1.9-mm-thick sheets by first punching rhomboidal holes to obtain a perforated sheet and then folding this sheet node row by node row to obtain regular pyramids as shown in Fig. 5. The sandwich plates were then assembled by laser welding rectangular sheets of dimensions $120.7 \times 127 \times 1.5\,mm^3$ to pyramidal core truss panels comprising 3×3 cells (Fig. 4). Unlike the 304 stainless steel which could be cut, folded and welded in its as-received state, the 6061-T6 aluminum alloy sheets were annealed to the O-condition prior to the perforation and folding operation. The pyramidal Al 6061 trusses were then solution treated and aged to return them to their peak strength condition (T6 condition) and then laser welded to the 6061-T6 aluminum face sheets.

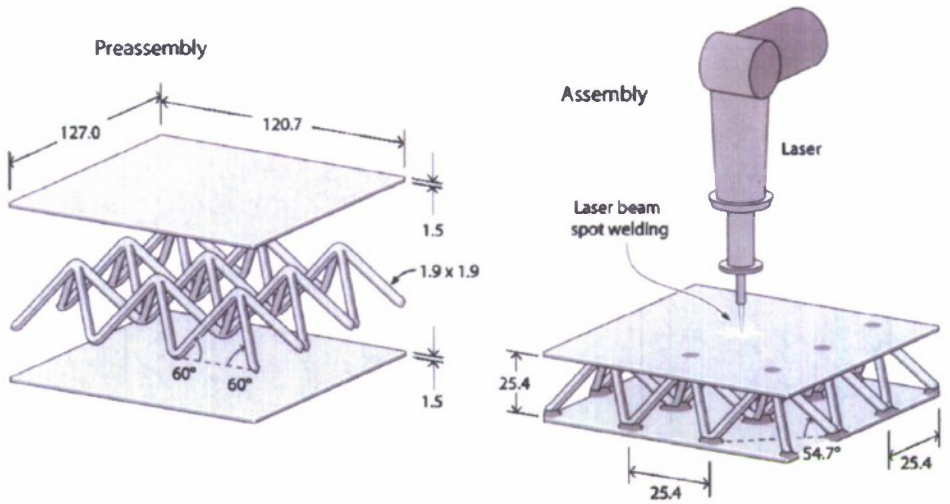

Fig. 4. Illustration of the laser welding process for bonding the pyramidal truss lattice to sandwich plate face sheets. Details of the dimensions of the sandwich plate and the core are included in the figure. All dimensions are in mm.

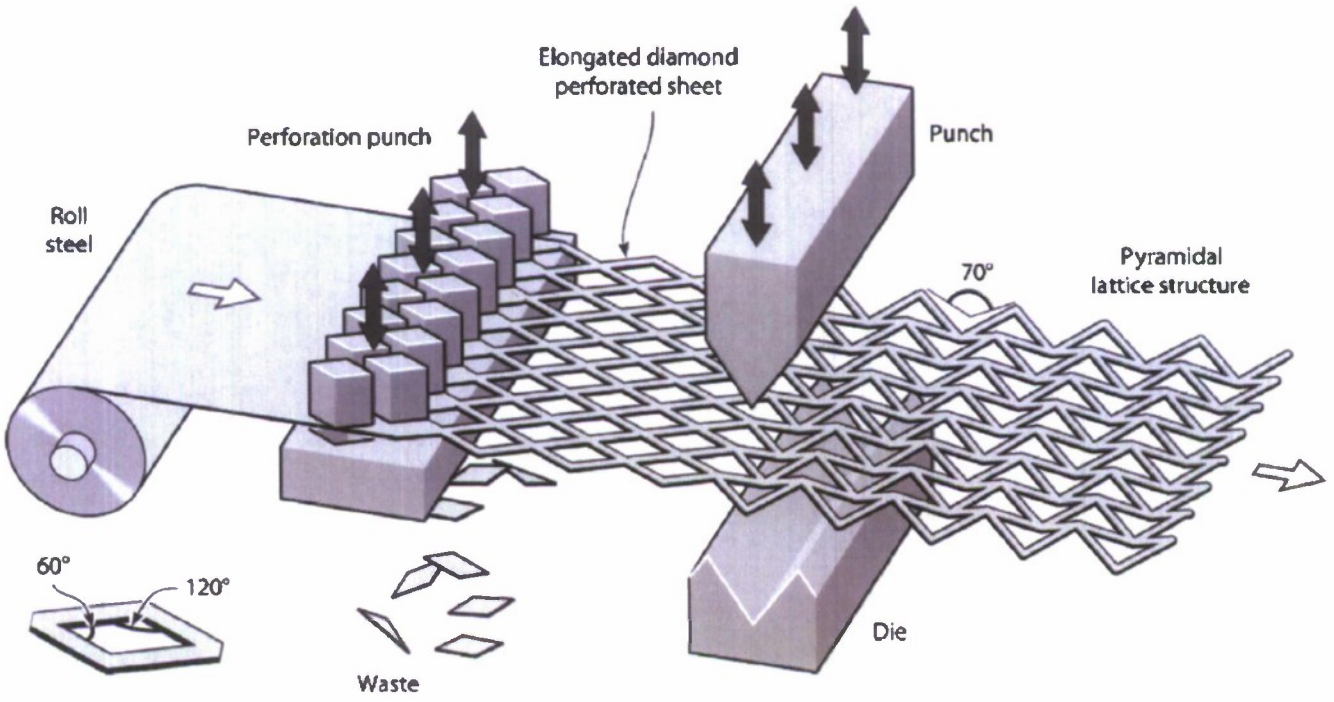

Fig. 5. Sketch of the punching and folding operation to manufacture the pyramidal truss lattice core.

3.2. Mechanical properties of the parent materials

Tensile specimens of dog-bone geometry were cut from each of the as-received steel and aluminum sheets. The uniaxial tensile responses of the 304 stainless-steel and Al 6061-T6 alloys at an applied strain rate of $10^{-3}\,s^{-1}$ are plotted in Fig. 6 using axes of true stress and logarithmic strain. We note that the key difference between the two alloys is their strain hardening capacity: while the 304 stainless steel displays a linear hardening post-yield response with a tangent modulus $E_t \approx 1$ GPa, the aluminum alloy exhibits an almost ideally plastic response. This enhanced strain hardening capacity of the stainless steel also stabilizes the tensile specimens against necking, resulting in the higher tensile ductility of the stainless steel compared to the 6061-T6 aluminum alloy.

3.3. Ballistic test methodology

The ballistic performance of the 304 stainless-steel and aluminum alloy sandwich plates was investigated for projectile impact velocities in the range

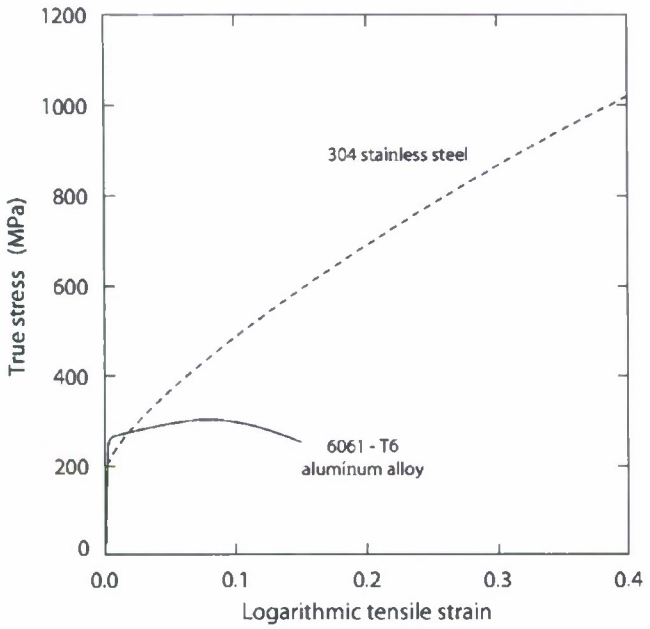

Fig. 6. Measured quasi-static uniaxial stress versus strain curves for the as-received 304 stainless-steel and 6061-T6 aluminum alloys.

$225\,\mathrm{m\,s^{-1}} \leqslant v_p \leqslant 1225\,\mathrm{m\,s^{-1}}$. In addition, for comparison purposes, we also investigated the ballistic performance of a $H = 3$-mm-thick 304 stainless-steel monolithic plate: this plate has an areal mass $m = 24\,\mathrm{kg\,m^{-2}}$ which is about 18% less than the steel sandwich plates (but was the same as the combined mass of the two face sheets of the steel sandwich plates). Impact experiments were performed on 15 sandwich plates of each alloy and 11 monolithic steel plates. In all cases, the plates were impacted at mid-span by a spherical, plain carbon steel projectile of diameter 12.5 mm weighing approximately 8 g.

Ballistic testing was conducted using a powder gun comprising a breech and a gun barrel as sketched in Fig. 7. The gun propelled plastic sabots carrying the 12.5 mm spherical steel projectiles. The operation of the gun is briefly described here. An electric solenoid activated a firing pin which initiated 0.38 caliber blank cartridges (Western Cartridge Company, East Alton, IL). The mixture of solid smokeless propellant IMR 3031, manufactured by IMR (Shawnee Mission, KS) and cotton (Fig. 7) in the breech was ignited by this charge and the expanding propellant gas accelerated the sabot through the gun barrel. The purpose of the cotton was to ensure the ensuing pressure wave remained uniform throughout deflagration of the propellant. The sabot was located

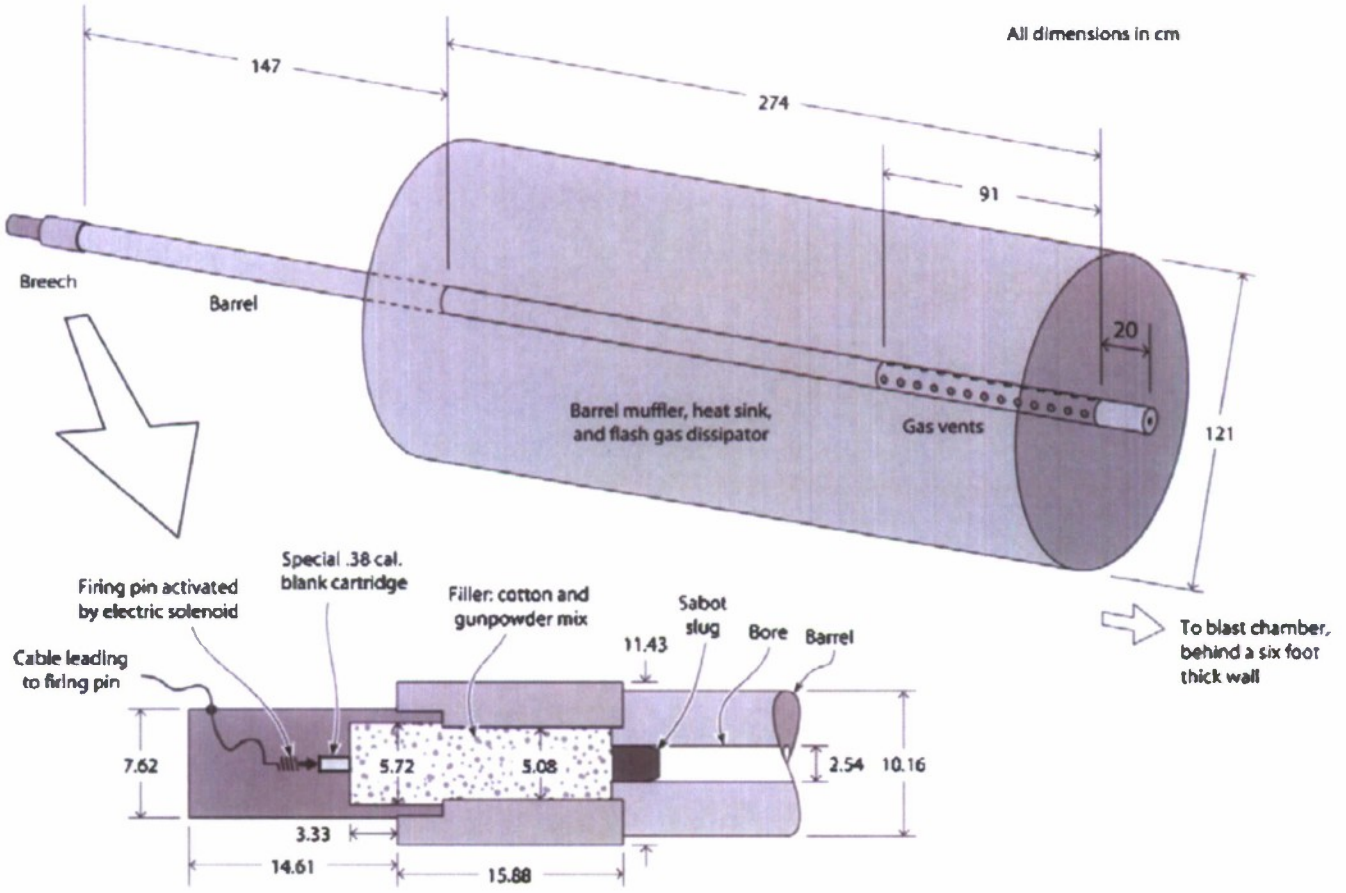

Fig. 7. Sketch showing the principal components of the single-stage powder gun employed in this study. The inset shows the breech arrangement along with the initial section of the gun barrel with the sabot slug that carries the 12.5-mm-diameter spherical steel projectile.

within a 25.4 mm bore gun barrel: a series of holes placed along the gun barrel were used to dissipate the shock wave and maintain a smooth acceleration of the sabot until it exited the barrel. The velocity at which the sabot exited the gun barrel was adjusted by selecting an appropriate quantity of gunpowder. The plastic sabot comprised four quarters that, upon mating, surrounded the 12.5 mm diameter spherical projectile. The sabot plugs had an inner diameter of 1.8 cm, an outer diameter of 2.7 cm, a height of 3.5 cm and a weight of 18.6 ± 0.12 g. Separation of the sabot from the projectile by air drag was facilitated by a 40° bevel at the sabot opening. The 12.5 mm diameter spherical steel projectiles weighed $M = 8.42 \pm 0.02$ g and were manufactured by National Precision Ball (Preston, WA) from 1020 plain carbon steel: the ultimate tensile strength of this steel is approximately 375 MPa [20].

3.4. Dynamic test protocol

The sample test fixture was located within a blast chamber (Fig. 8). A square, 40-cm-long, 2.86-cm-thick steel plate was located 1 m from the end of the barrel. It had a 3.8 cm diameter hole located in the center through which the projectile entered the test area. Two pairs of brake screens were used to measure the projectile entry and exit velocities (Fig. 8) and provided impact and exit velocities measurements with a precision of $\pm 2.0\,\mathrm{m\,s^{-1}}$. The test samples were edge clamped along the top and bottom edges so that the effective span of the plate between the clamped edges was approximately 110 mm while the width of the plate was 120 mm; see Fig. 8. The kinetic energy of the projectile dissipated by the sandwich panel structures depends upon the way in which the projectile interacts with the truss cores. To remove any source of variability in the measurements, the sandwich panels were carefully positioned so that the projectile impacted at the center of the square formed by four nodes of the truss on the face sheet facing the incoming projectile (see Fig. 4). The projectile usually impacted the back face sheet at the apex of a truss. High-speed photography was used to observe the dynamic transverse deformation and failure of the plates. An Imacon 200 digital framing camera was used for this purpose; this camera is capable of taking up to 16 frames at a maximum rate of 10^8 frames $\mathrm{s^{-1}}$. Inter-frame times in the range 4.5–50 μs were employed and the exposure time was 300 ns. In addition, the plates were examined after each experiment to understand the failure mechanisms.

4. Summary of observations

We proceed to detail the observations in two steps. First we summarize the ballistic performance of the sandwich and monolithic plates and then proceed to discuss the critical failure and deformation mechanisms as observed via high-speed photography and post-test examination of the test specimens.

4.1. Ballistic performance

4.1.1. Stainless-steel plates

The measured projectile exit or residual velocity v_r as a function of the impact velocity v_p is plotted in Fig. 9a for the 304 stainless-steel sandwich panels. Full penetration of the 304 stainless-steel sandwich panels occurred at impact velocities greater than $v_p = v_{crit} \approx 415\,\mathrm{m\,s^{-1}}$. This is defined as the ballistic limit of these panels for the projectile used in this investigation. Consistent with the predictions discussed in Section 2, a sharp increase in the projectile residual velocity is observed just above the ballistic limit. In spite of this, the sandwich panel does retard the projectile significantly: a projectile that impacted with a velocity of $v_p = 481\,\mathrm{m\,s^{-1}}$ exited the sandwich plate at $v_r = 266\,\mathrm{m\,s^{-1}}$. We define χ as the energy absorbed by the sandwich panel per unit areal mass m of the plate:

$$\chi \equiv \frac{M}{2m}(v_p^2 - v_r^2), \tag{1}$$

where M is the mass of the projectile (the high-speed photographs shown subsequently indicate that while the projectile may undergo significant deformation during the impact event, the projectile remains intact and thus retains all its original mass M). The measured variation of χ with v_p is included in Fig. 9b for the steel sandwich plates. Below the critical penetration velocity v_{crit}, the sandwich panel absorbs all the kinetic energy of the projectile, i.e. $\chi = Mv_p^2/(2m)$. The absorbed energy drops slightly at the onset of penetration, as the projectile shears through and prevents additional energy absorption by tensile stretching as discussed in Section 2. The energy absorption capacity of the sandwich plates continues to increase for $v_p > v_{crit}$: the mechanisms for this phenomena are discussed in Sections 4.2 and 4.3.

The residual velocity measurements and corresponding energy absorption data for the 304 stainless-steel monolithic plate are also included in Figs. 9a and b. Penetration occurred at about the same impact velocity as the sandwich structure and subsequently the residual velocity increased sharply. The residual velocity measurements in Fig. 9a suggest that for a given projectile velocity above the ballistic limit, the monolithic plate absorbs slightly less of the kinetic energy of the projectile compared to the sandwich plate. However, recall that the sandwich plate is 18% heavier than the monolithic plate. In terms of the energy absorption per unit areal mass of the plates (Fig. 9b), the ballistic performance of the sandwich and monolithic steel plates are experimentally indistinguishable.

4.1.2. Aluminum plates

The residual velocity versus impact velocity data for the 6061-T6 aluminum alloy sandwich plates are plotted in Fig. 10a. The lowest value of v_p achievable in the powder gun employed in this study was approximately $230\,\mathrm{m\,s^{-1}}$: complete penetration of the sandwich plate occurred at this value of v_p and thus the ballistic limit could not be

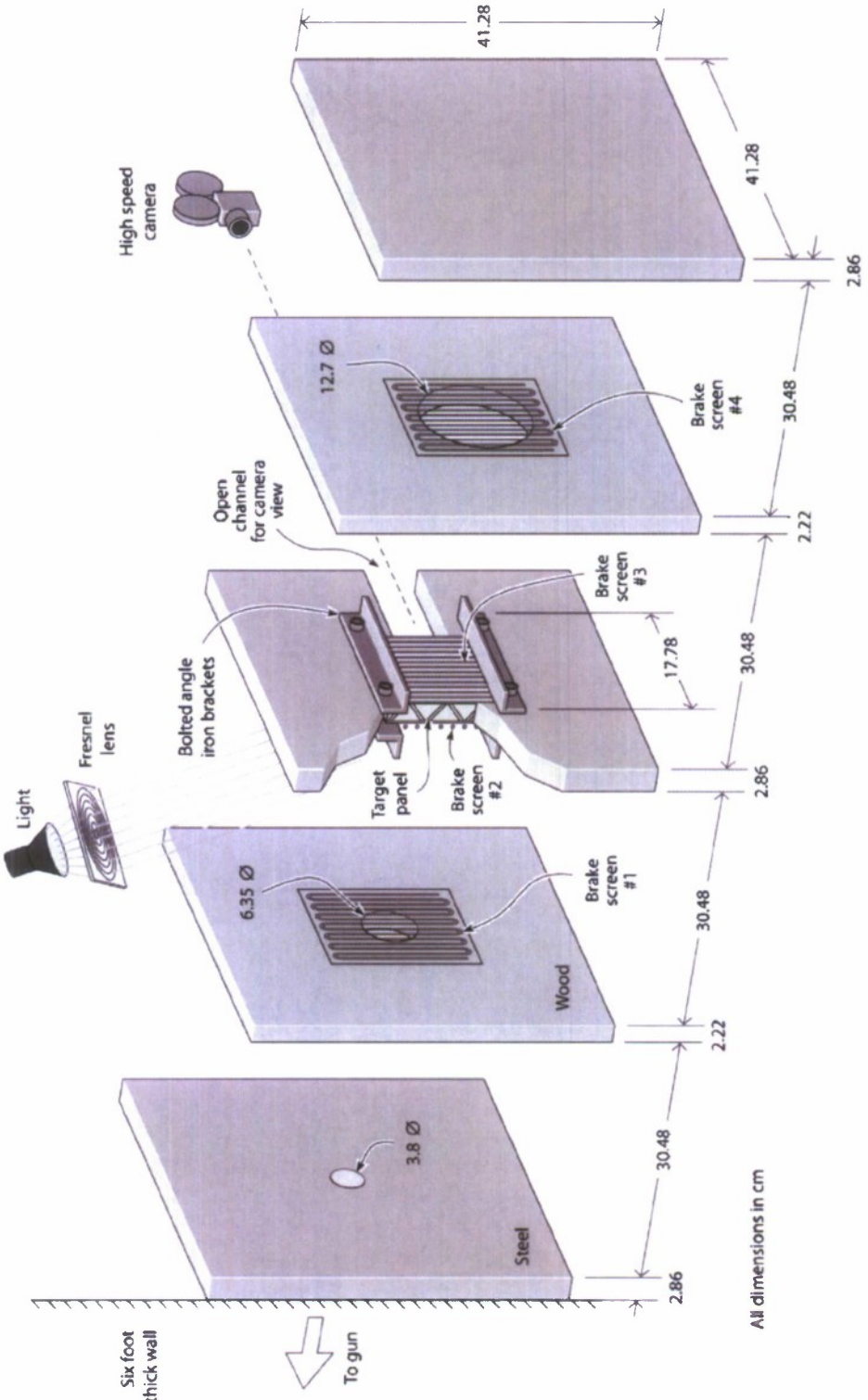

Fig. 8. Schematic illustration of the test set-up including the location of the fixture that holds the specimen, the brake screens, the high-speed camera, the light source and the projectile catching arrangement.

accurately ascertained for the aluminum sandwich plates. For comparison purposes, the stainless-steel sandwich data of Fig. 9a are included in Fig. 10a and clearly demonstrates the superior ballistic performance of the steel plate compared to the aluminum sandwich plate with an identical geometry (and volume). A comparison of the energy absorbed per unit areal mass of the 304 stainless-steel and 6061-T6 aluminum plates is included in Fig. 10b.

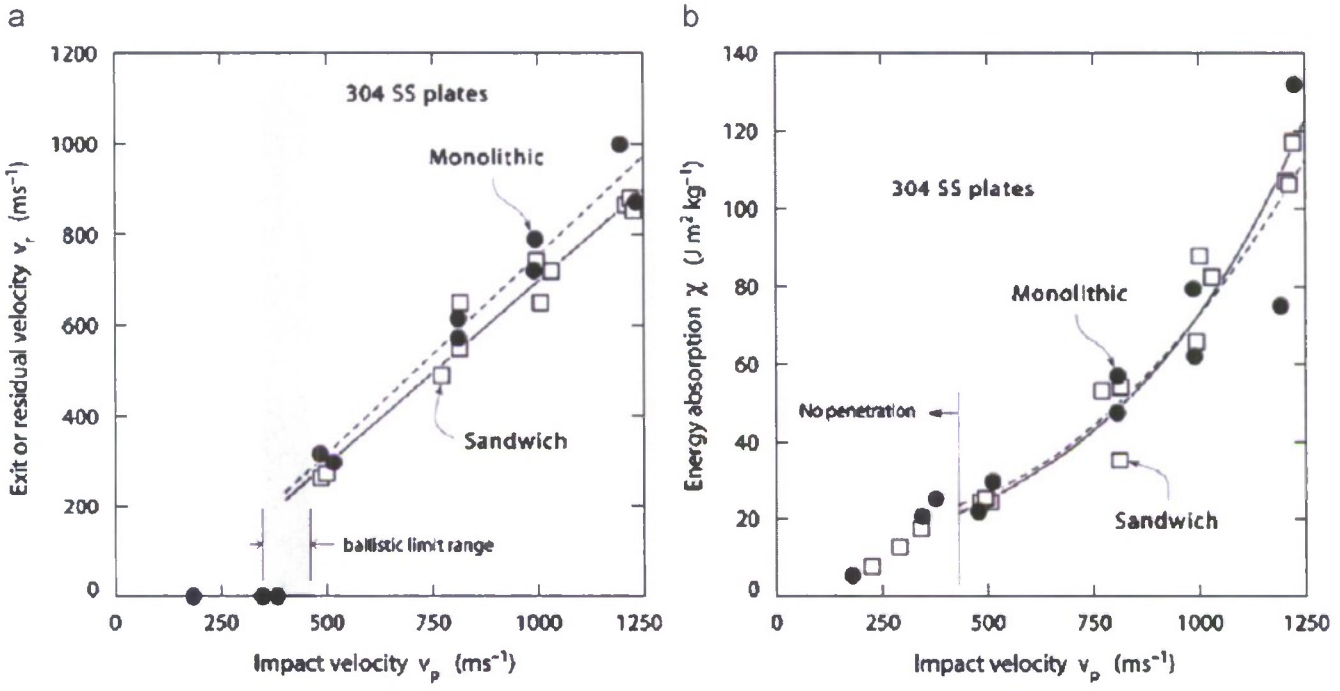

Fig. 9. Measurements of (a) the projectile exit velocity v_r and (b) χ which is defined as the loss in the projectile kinetic energy per unit areal mass of the plate as a function of the initial projectile velocity v_p. Data are shown for the 304 stainless-steel monolithic and sandwich plates.

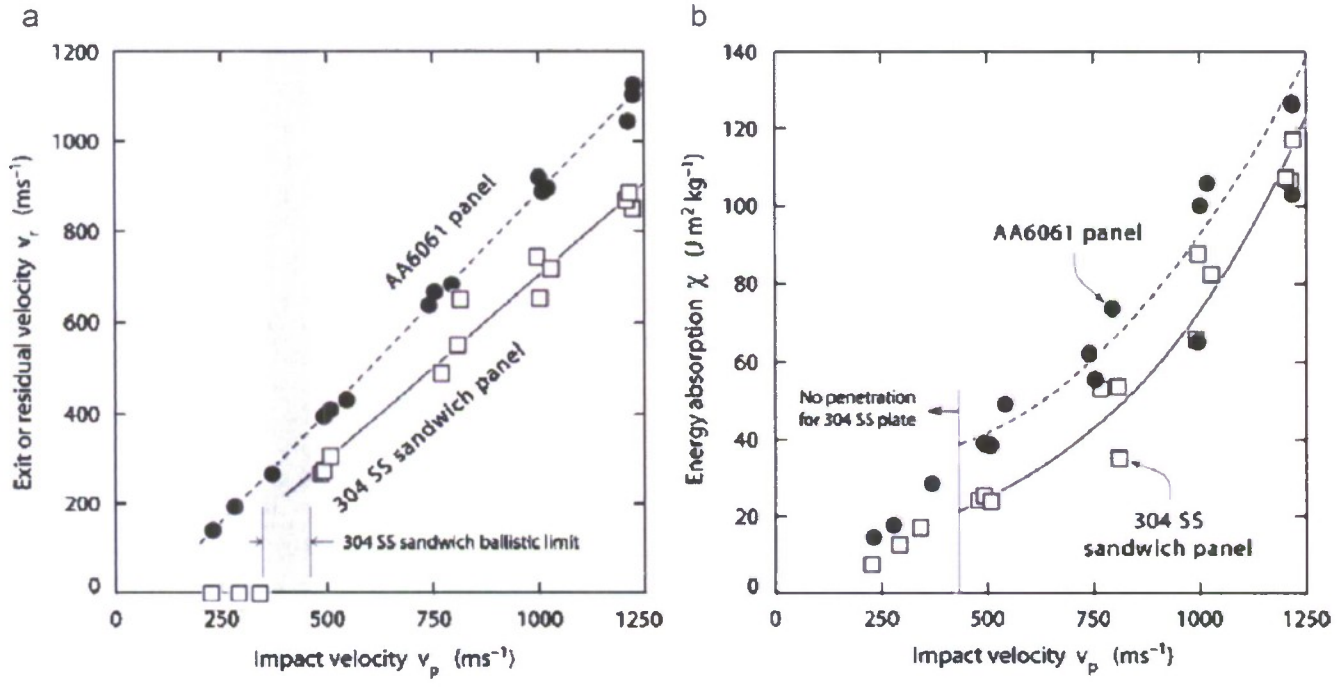

Fig. 10. Measurements of (a) the projectile exit velocity v_r and (b) χ which is defined as the loss in the projectile kinetic energy per unit areal mass of the plate as a function of the initial projectile velocity v_p. Data are shown for the 6061-T6 and 304 stainless-steel sandwich plates.

These data indicate that consistent with the arguments presented in Section 2, on a unit mass basis the aluminum sandwich plates outperform the steel plates as the aluminum has approximately the same yield strength as the steel but has a density approximately one-third that of steel. The results presented here seem to suggest that the higher strain hardening capacity and failure strain of the stainless steel do not compensate for its higher density resulting in the aluminum having a superior ballistic performance on a per mass basis.

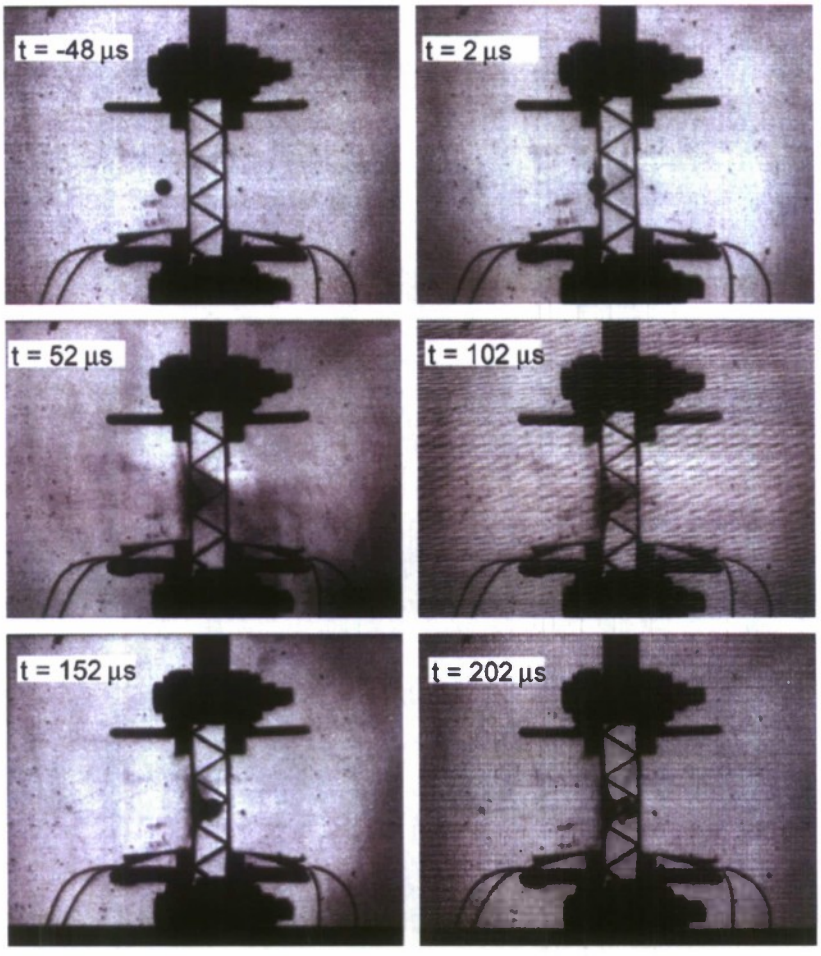

Fig. 11. High-speed photographic sequence (exposure time 300 ns) of the impact of the 304 stainless-steel sandwich plate by the projectile at $v_p = 290\,m\,s^{-1}$. Time after the impact of the projectile against the proximal face sheet is indicated for each frame.

4.2. *High-speed photographic sequences of the impact events*

A sequence of high-speed photographs of the deformation and failure modes associated with the impact of the spherical projectile against the stainless-steel sandwich plates are included in Figs. 11–13 for $v_p = 290$, 768 and $1206\,m\,s^{-1}$, respectively. The timing of each photograph is marked on the figures with $t = 0$ taken as the instant of the impact against the proximal or front face sheet. At $v_p = 290\,m\,s^{-1}$, the projectile penetrates the proximal face at $t = 52\,\mu s$ and is completely arrested by the distal face sheet at $t = 102\,\mu s$. The photographs also confirm the accuracy of the positioning of the plates, i.e., the projectile impacts the proximal surface at approximately the center of the square base a pyramidal unit cell and consequently the projectile impacted the apex or node of this pyramidal unit cell at the distal face sheet.

Consistent with the basic supersonic flow theory [21], at $v_p = 768\,m\,s^{-1}$ (i.e. Mach number $M_\infty \equiv v_p/c \approx 2.25$, where $c = 340\,m\,s^{-1}$ is the velocity of sound in the undisturbed air), a detached shock wave is formed in front of the sphere (see photo at time $t = -18\,\mu s$ in Fig. 12) with a shock wave angle[1] greater than the Mach angle $\omega = \sin^{-1}(c/v_p)$. The projectile penetrates the proximal face and the reflected air shocks from the proximal face sheet are clearly visible for $t \geqslant 22\,\mu s$. There seem to be two distinct regimes in the reflected shock: (i) a dark cloud immediately adjacent to the proximal face sheet; we believe that this cloud is caused by tiny fragments associated with the shear failure of the face sheet and (ii) strong reflected air shock where the density of the air rises sufficiently to cause a significant change in the refractive index of the air. The projectile impacts the distal face sheet at $t = 32\,\mu s$ and completely penetrates the sandwich plate by $t = 82\,\mu s$. The air shock reflected from the distal face sheet interacts with the truss core resulting in a significant pressure rise that causes the ionization of the air trapped between the two face sheets of the sandwich plate. This ionization manifests itself in the photographs as a bright light as seen for

[1]The shock wave angle is the angle that the shock wave makes with the direction of motion of the projectile.

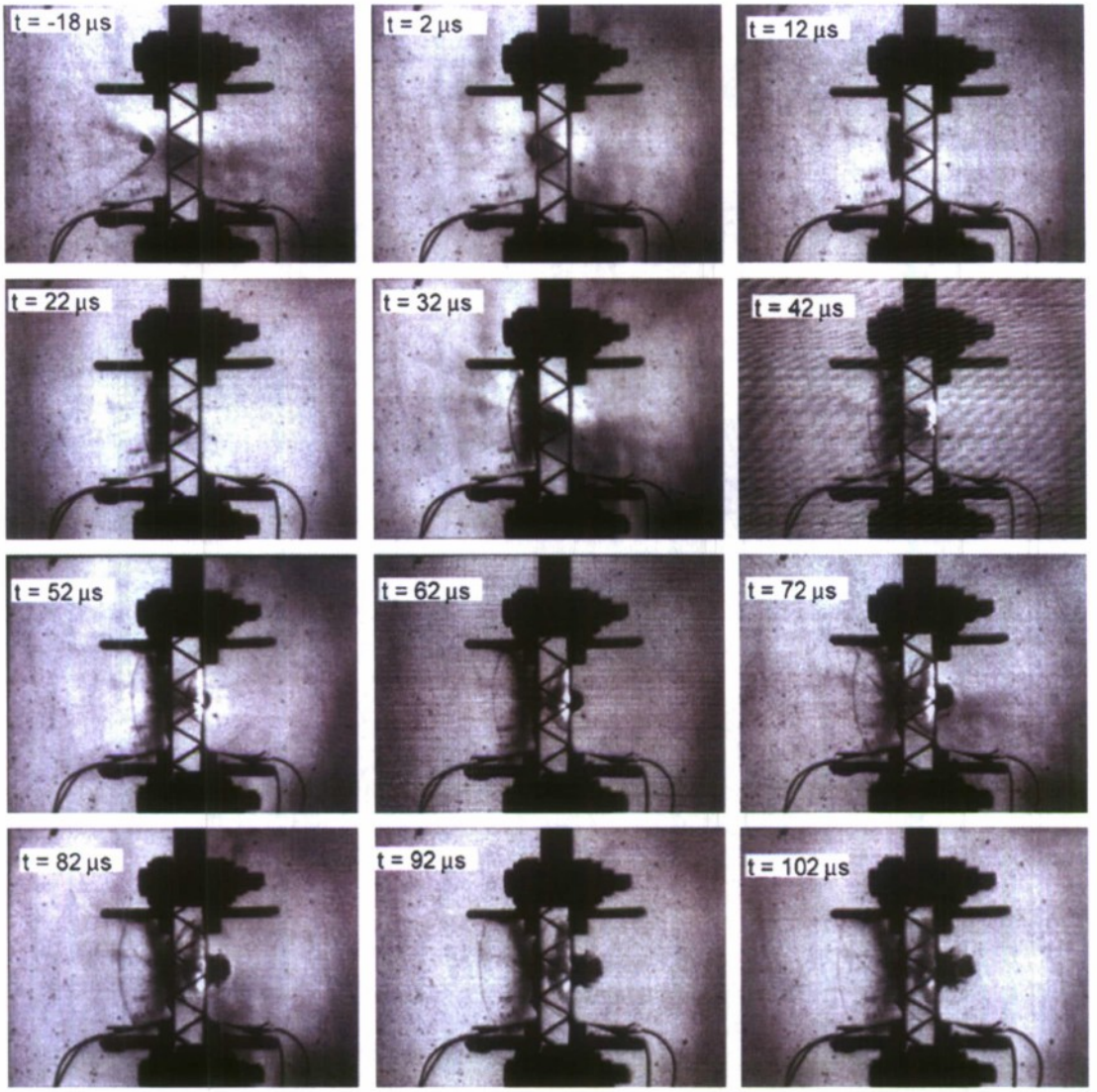

Fig. 12. High-speed photographic sequence (exposure time 300 ns) of the impact of the 304 stainless-steel sandwich plate by the projectile at $v_p = 768\,m\,s^{-1}$. Time after the impact of the projectile against the proximal face sheet is indicated for each frame.

$42\,\mu s \leqslant t \leqslant 82\,\mu s$. (Fractoluminescence[2] is not thought to be the source of this bright light as the bright spot spreads slowly to locations where no damage of the specimen was observed by post-test examination.) In the photographic sequence for $v_p = 1206\,m\,s^{-1}$ (Fig. 13) we again observe an oblique air shock associated with the incoming projectile and consistent with supersonic flow theory, the shock angle is smaller than that for the $v_p = 768\,m\,s^{-1}$ case. Moreover, the detached air shock ahead of the spherical projectile is now sufficiently strong that ionization of the air is observed both on the outer surface of the proximal face sheet and within the sandwich plate.

High-speed photographs of the penetration of the 3-mm-thick monolithic steel plate ($v_p = 1192\,m\,s^{-1}$) and the aluminum sandwich plate ($v_p = 1222\,m\,s^{-1}$) are included in Figs. 14 and 15, respectively. The detached shock wave in front of the incoming projectile is clearly seen in both figures along with the bright patches associated with the ionization of air as the shock wave reflects off the plates. While the failure mechanism of the aluminum plate is similar to the steel sandwich plate at a similar value of v_p, it is clear on comparing Figs. 13 and 15 that the projectile travels through the aluminum sandwich plate at a significantly higher velocity compared to its transit velocity through the steel sandwich plate. It is also worth noting that even though shear-off is the penetration of monolithic plate at $v_p = 1192\,m\,s^{-1}$, the high-speed photographs indicate this failure is accompanied by some fragmentation: these fragments are seen to follow in the wake of the projectile in Fig. 14.

The high-speed photographs discussed here clearly show that the air shocks associated with the high-velocity

[2]Fractoluminescence is the emission of light from the fracture of a crystal.

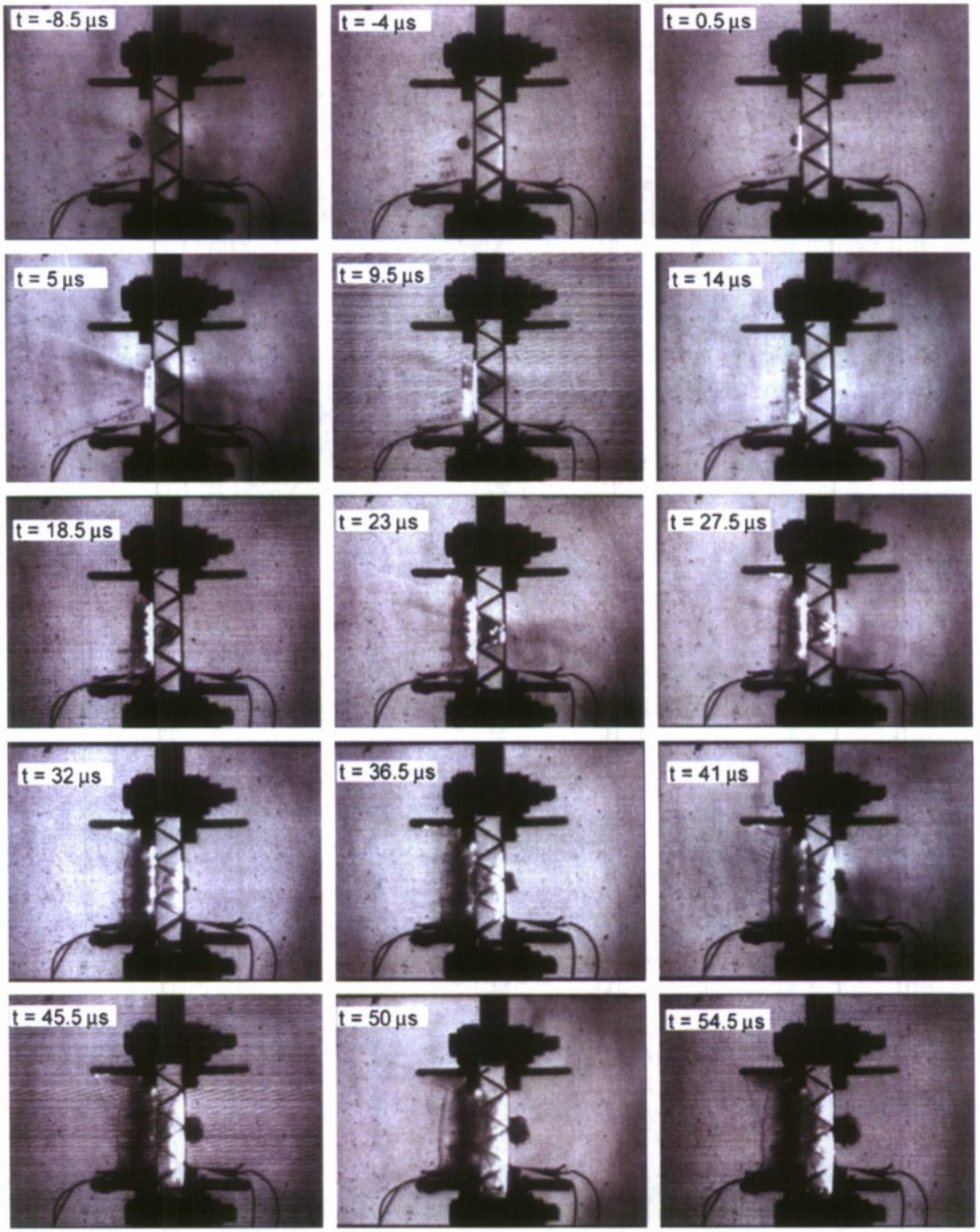

Fig. 13. High-speed photographic sequence (exposure time 300 ns) of the impact of the 304 stainless-steel sandwich plate by the projectile at $v_p = 1206\,m\,s^{-1}$. Time after the impact of the projectile against the proximal face sheet is indicated for each frame.

projectiles are sufficiently strong that their reflection from the structures causes ionization of air. This ionization is more severe when the projectile impacts the distal face sheet of the sandwich plate presumably due to the multiple reflections of the shock waves from the inner surfaces of the distal and proximal face sheets of the sandwich plate (such reflections are of course absent for the monolithic plate and hence smaller levels of ionization are observed; compare Figs. 13 and 14). While calculating the energy absorption capacities of the structures (Figs. 9b and 10b), the reduction in the kinetic energy of the projectile was attributed completely to deformation and failure of the plates (Eq. (1)). The significance of additional energy dissipation mechanisms

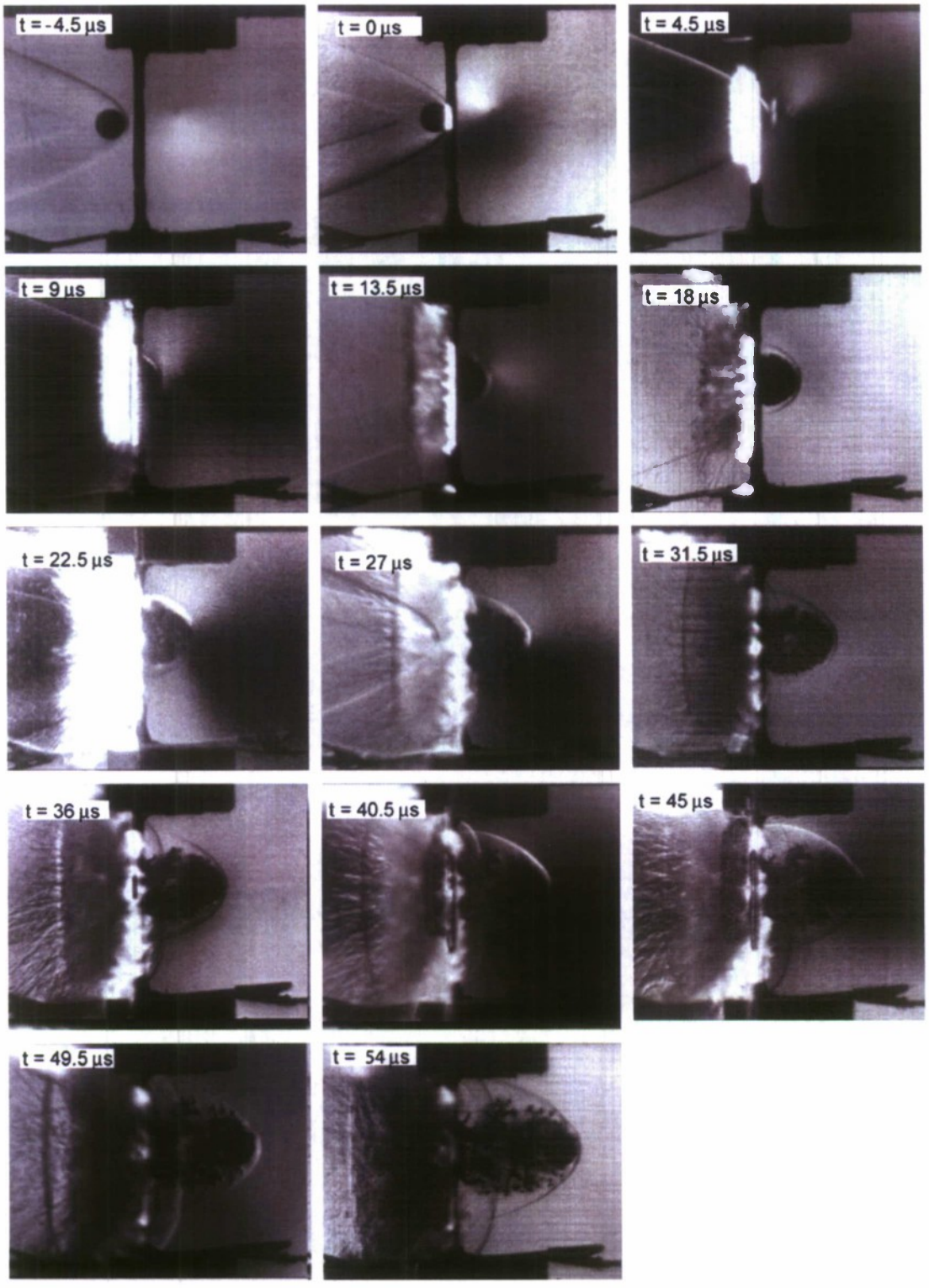

Fig. 14. High-speed photographic sequence (exposure time 300 ns) of the impact of the 304 stainless-steel monolithic plate by the projectile at $v_p = 1192\,\mathrm{m\,s^{-1}}$. Time after the impact of the projectile is indicated for each frame.

such as those associated with the ionization of the air is at present unclear and additional studies performed in evacuated chambers would be required to quantify these contributions.

4.3. *Deformation and fracture mechanisms*

In order to gain some insight into the deformation and fracture mechanisms, some of the tested monolithic and

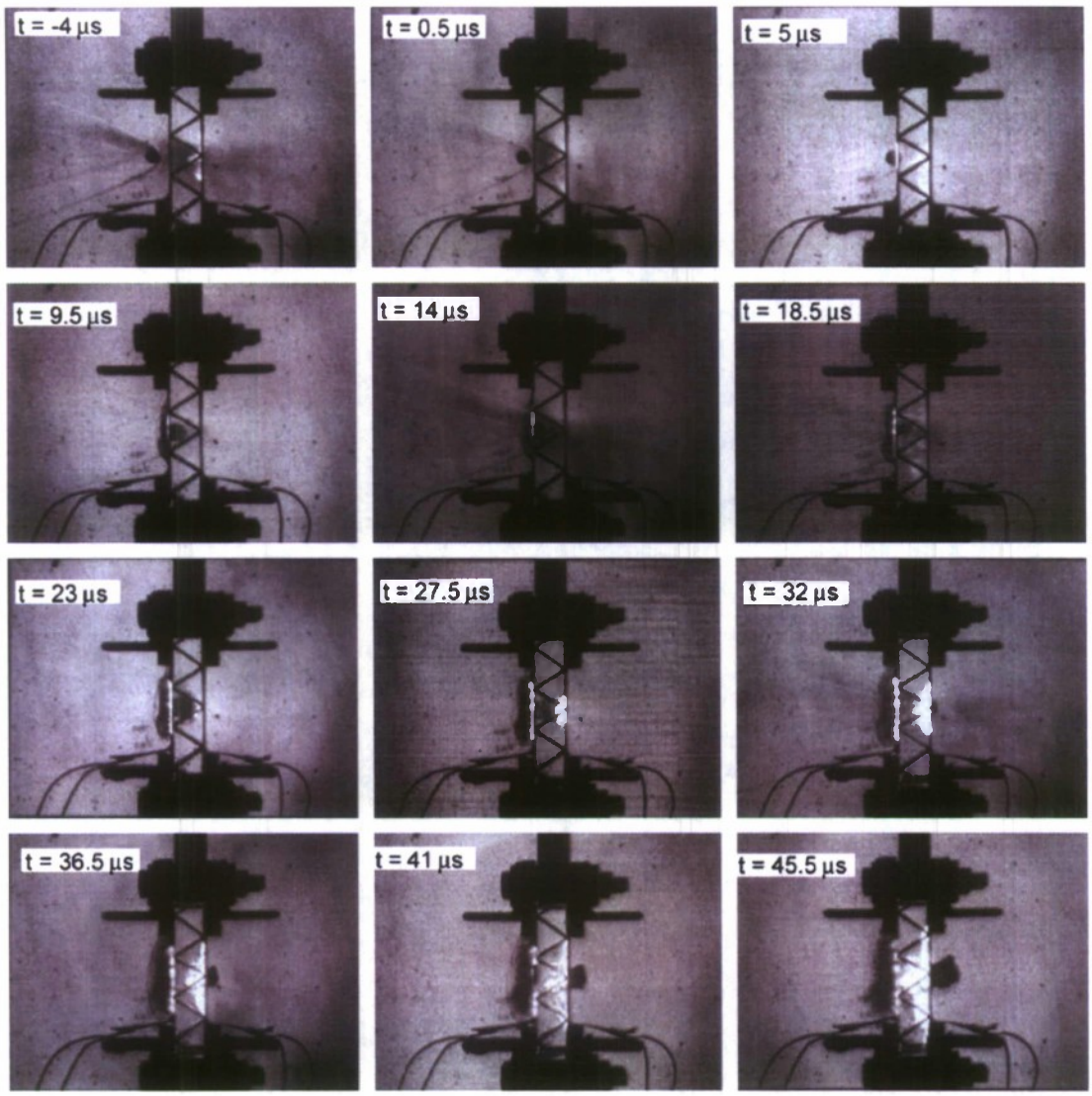

Fig. 15. High-speed photographic sequence (exposure time 300 ns) of the impact of the 6061-T6 sandwich plate by the projectile at $v_p = 1222\,m\,s^{-1}$. Time after the impact of the projectile against the proximal face sheet is indicated for each frame.

sandwich plates were sectioned along their mid-plane and photographed. We discuss the key features that emerge from these photographs.

4.3.1. Stainless-steel plates

Photographs of the sandwich plate impacted at $v_p = 340$ and $1206\,m\,s^{-1}$ are included in Figs. 16a and b, respectively. First consider the $v_p = 340\,m\,s^{-1}$ case. Penetration of the proximal or front face sheet resulted in an entry hole approximately 12.5 mm in diameter and a bending deflection of 6.5 mm. In line with the penetration model [19], the low rate of loading enabled the face sheet to undergo simultaneous bending and shearing deformations: plastic bending and stretching occurred over a region approximately 3 cm in diameter before penetration occurred by a shear-off process. The rear or distal face sheet underwent more extensive bending and stretching which was accompanied by truss stretching and fracture of some of the nodes of the pyramidal truss core. Though the distal face sheet began to fail by a petalling mechanism associated with extensive stretching, the projectile was fully arrested by the sandwich plate. A key observation is the switch in the failure modes between the proximal and distal face sheets: shear-off is the failure mechanism for the proximal face but the reduction in the projectile velocity that occurs in this process results in tensile failure being the operative mode on the distal face sheet.

Next consider the case with $v_p = 1206\,m\,s^{-1}$ (Fig. 16b). At this high impact velocity, the projectile penetrates the proximal face sheet by shear-off so rapidly that there is negligible associated plastic bending or stretching of the face sheet. However, in contrast to the shear-off at $v_p = 340\,m\,s^{-1}$, the diameter of the hole created by the projectile in this case is greater than the diameter of the

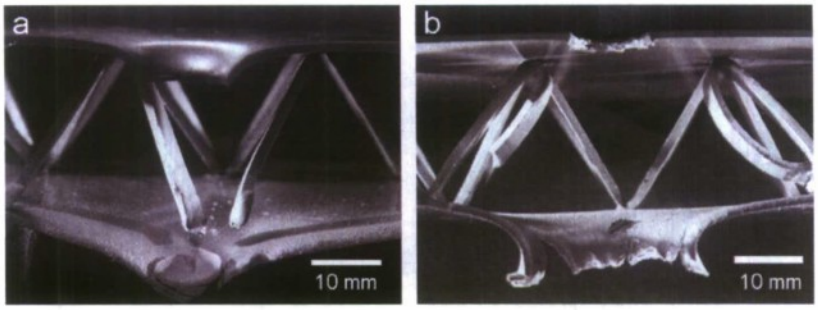

Fig. 16. Photographs of the 304 stainless-steel sandwich plates impacted at (a) $v_p = 340\,m\,s^{-1}$ and (b) $v_p = 1206\,m\,s^{-1}$. The photographs were taken after sectioning the plates along their mid-plane.

projectile. This mode is known as ductile hole enlargement [13]: the observed thickening of the plate around the failure surface is associated with this hole enlargement process. The reduction in the projectile velocity by this shear-off mechanism causes a sufficient reduction in the projectile velocity so that tensile tearing is again the operative failure mode for the distal face sheet.

Photographs of the deformation and failure mechanisms of the $H = 3$ mm monolithic steel plate are included in Fig. 17 for three selected values of v_p. At $v_p = 340\,m\,s^{-1}$, the plate arrested the projectile and significant plastic bending and stretching of the plate is observed along with some shearing near the edge of the contact between the spherical projectile and plate. The maximum deflection of the plate was 9.5 mm. At $v_p = 805\,m\,s^{-1}$, the projectile penetrated the face leaving a 12.5-mm-diameter hole. Adiabatic shearing seems to have been the failure mechanism though this shear failure was accompanied by some bending and stretching of the plate resulting in a 6.5 mm deflection of the plate. At a high impact velocity of $v_p = 1226\,m\,s^{-1}$, the projectile penetrated the steel plate by shear-off with no associated plastic bending or stretching of the plate. The projectile created a hole in the plate 15.9 mm in diameter with thickening of the plate around the failure surface, i.e., ductile hole enlargement was the operative failure mechanism.

A key difference between the failure mechanisms of the monolithic and sandwich plates is that unlike the sandwich plates, the monolithic plates never displayed a petalling mode of failure. At the highest velocities investigated here, the monolithic plates failed by a shear-off mode with some associated ductile hole enlargement. By contrast, this failure mode was only observed on the proximal face sheet of the sandwich plates with the distal face sheet undergoing a petalling failure mode due to the reduction in the projectile velocity by the proximal face sheet. These failure mode differences however did not result in any appreciable differences in the ballistic performance of the two systems (Fig. 9).

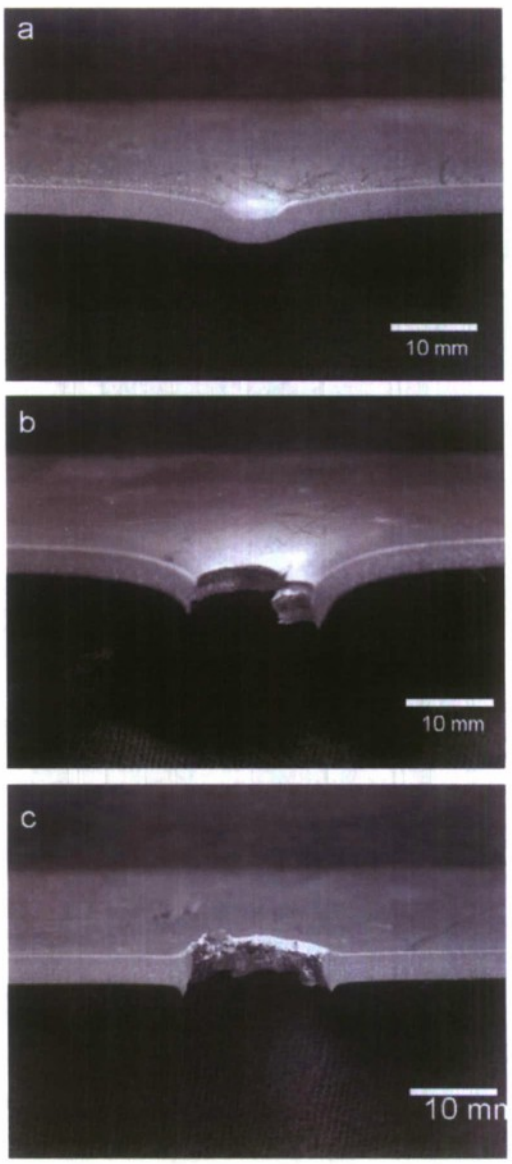

Fig. 17. Photographs of the 304 stainless-steel monolithic plates impacted at (a) $v_p = 340\,m\,s^{-1}$, (b) $v_p = 805\,m\,s^{-1}$ and (c) $v_p = 1226\,m\,s^{-1}$. The photographs were taken after sectioning the plates along their mid-plane.

4.3.2. *Aluminum plates*

Photographs of the deformed/failed aluminum sandwich plates impacted at $v_p = 280$ and $1222\,m\,s^{-1}$ are included in Figs. 18a and b, respectively. Similar to the stainless-steel sandwich plates, a petalling-type failure was observed on the distal face sheet while a shear-off failure occurred on the proximal face sheet. Moreover, similar to the steel

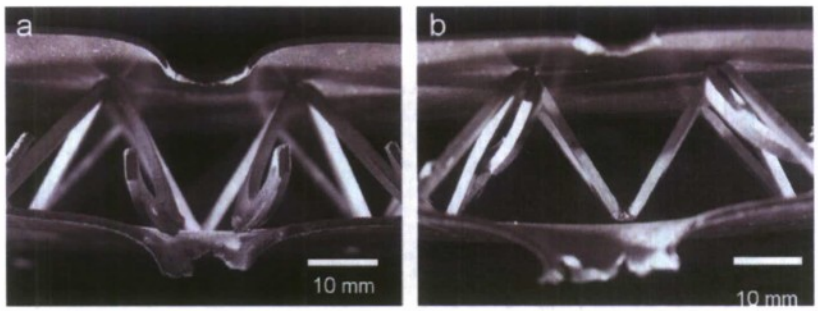

Fig. 18. Photographs of the 6061-T6 aluminum sandwich plates impacted at (a) $v_p = 280\,m\,s^{-1}$ and (b) $v_p = 1222\,m\,s^{-1}$. The photographs were taken after sectioning the plates along their mid-plane.

sandwich plates, at the lower impact velocities, shear-off failure of the proximal face sheet occurred after significant plastic bending and stretching while shear-off accompanied by hole enlargement but negligible plate bending occurred at the higher impact velocities. Thus, the deformation and failure mechanisms of the aluminum sandwich panels were similar to the steel panels: we attribute the superior ballistic performance of the aluminum panels on a unit mass basis (Fig. 10) to the higher value of σ_Y/ρ for aluminum compared to steel (cf. Section 2).

5. Concluding remarks

Clamped sandwich plates with a pyramidal truss core and monolithic plates of approximately equal areal mass were impacted by a spherical steel projectile at velocities ranging from 250 to 1300 ms^{-1}. Structures made from both 304 stainless-steel and the 6061-T6 aluminum alloy were tested and the ballistic performance quantified by measuring both the entry and exit velocities of the projectiles.

(i) The ballistic performance of the 304 stainless-steel sandwich plates is superior to the 6061-T6 aluminum alloy plates on a per volume basis. However, the data presented here suggest that the aluminum plates outperform the steel plates on a per mass basis due to the higher value of strength to density ratio, σ_Y/ρ, of the aluminum.

(ii) The ballistic performance of the steel sandwich and monolithic plates of equal mass was almost indistinguishable.

(iii) At impact velocities exceeding Mach 2, the detached air shock in front of the spherical projectile ionizes the air around the structure during the impact event. The significance of this "blast" wave associated with the projectile is as yet unclear.

Numerous studies over the last few years have demonstrated the superior blast resistance of sandwich plates compared to monolithic plates of equal mass, e.g. [1,2]. The data presented here suggest that distributing the mass of a monolithic plate into a sandwich plate does not have an adverse effect on the ballistic performance of the structures suggesting that sandwich plates outperform monolithic plates for multi-functional applications that require structural efficiency combined with blast resistance and ballistic performance.

Acknowledgments

The ballistic measurements were supported by the Defense Advanced Research Projects Agency and the Office of Naval Research under Grant number N00014-04-1-0299 (Dr. Leo Christodoulou was its program manager). The analysis work has been performed as part of the *Ultralight Metallic Panels with Textile Cores Designed for Blast Mitigation and Load Retention* program conducted by the University of Virginia and Cambridge University and funded by the Office of Naval Research (ONR) under Grant number N00014-01-1-1051 (Drs. David Shifler and Steve Fishman were its program managers). *Distribution Statement "A" (Approved for Public Release, Distribution Unlimited).*

References

[1] Fleck NA, Deshpande VS. The resistance of clamped sandwich beams to shock loading. J Appl Mech, ASME 2004;71:386.

[2] Xue Z, Hutchinson JW. A comparative study of blast-resistant metal sandwich plates. Int J Impact Eng 2004;30:1283.

[3] Radford DD, Fleck NA, Deshpande VS. The response of clamped sandwich beams subjected to shock loading. Int J Impact Eng 2006;32:968.

[4] Rathbun HJ, Radford DD, Xue Z, He MY, Yang J, Deshpande VS, et al. Performance of metallic honeycomb-core sandwich beams under shock loading. Int J Solids Struct 2006;43:1746.

[5] Dharmasena KP, Wadley HNG, Xue Z, Hutchinson JW. Mechanical response of metallic honeycomb sandwich panels to high intensity dynamic loading. Int J Impact Eng, 2007, in Press, doi:10.1016/j.ijimpeng.2007.06.008.

[6] Ashby MF, Evans AG, Fleck NA, Gibson LJ, Hutchinson JW, Wadley HNG. Metal foams: a design guide. Oxford: Butterworth-Heinemann; 2000.

[7] Tilbrook MT, Radford DD, Deshpande VS, Fleck NA. The dynamic compressive response of the Y-frame and corrugated sandwich core. Int J Solids Struct 2007;44(18–19):6101.

[8] Corbett GG, Reid SR, Johnson W. Impact loading of plates and shells by free-flying projectiles: a review. Int J Impact Eng 1996; 18:141.
[9] Landkof B, Goldsmith W. Petalling of thin metallic plates during penetration by cylindro-conical projectiles. Int J Solids Struct 1985;21:245.
[10] Wierzbicki T. Petalling of plates under explosive and impact loading. Int J Impact Eng 1999;22:935.
[11] Bai YL, Johnson W. Plugging—physical understanding and energy absorption. Metals Technol 1982;9:182.
[12] Borvik T, Leinum JR, Solberg JK, Hopperstad OS, Langseth M. Observations on shear plug formation in Weldox 460 E steel plates impacted by blunt-nosed projectiles. Int J Impact Eng 2001;25:553.
[13] Backman M, Goldsmith W. The mechanics of penetration of projectiles into targets. Int J Eng Sci 1978;16:1.
[14] Almohandes A, Abdel-Kader M, Eleiche A. Experimental investigation of the ballistic resistance of steel-fiberglass reinforced polyester laminar plates. Composites B 1996;27B:447.
[15] Ben-Dor G, Dubinsky A, Elperin T. On the ballistic resistance of multi-layered targets with air gaps. Int J Solids Struct 1998;35:3097.
[16] Radin J, Goldsmith W. Normal projectile penetration and perforation of layered targets. Int J Impact Eng 1988;7:229.
[17] Goldsmith W, Wang G-T, Li K, Cane D. Perforation of cellular sandwich plates. Int J Impact Eng 1997;19:361.
[18] Zhao H, Elnasri I, Girad Y. Perforation of aluminum foam core sandwich panels under impact loading—an experimental study. Int J Impact Eng 2007;34:1246.
[19] Deshpande VS, Kazemahvazi S, Wadley HNG. Failure mechanism maps for the impact loading of clamped beams, 2007, submitted for publication.
[20] Metals handbook, vol. 1, 10th ed. Properties and selections: irons, steels and high performance alloys. Materials Park, OH: ASM International; 1990.
[21] Liepmann HW, Roshko A. Elements of gas-dynamics. New York: Dover Publications Inc.; 1985.